

# REPORT DOCUMENTATION PAGE

Form Approved  
OMB No. 0704-0188

Public reporting burden for this collection of information is estimated to average 1 hour per response, including the time for reviewing instructions, searching existing data sources, gathering and maintaining the data needed, and completing and reviewing this collection of information. Send comments regarding this burden estimate or any other aspect of this collection of information, including suggestions for reducing this burden to Department of Defense, Washington Headquarters Services, Directorate for Information Operations and Reports (0704-0188), 1215 Jefferson Davis Highway, Suite 1204, Arlington, VA 22202-4302. Respondents should be aware that notwithstanding any other provision of law, no person shall be subject to any penalty for failing to comply with a collection of information if it does not display a currently valid OMB control number. PLEASE DO NOT RETURN YOUR FORM TO THE ABOVE ADDRESS.

1. REPORT DATE (DD-MM-YYYY) 05-06-2007	2. REPORT TYPE Technical Paper	3. DATES COVERED (From - To)		
4. TITLE AND SUBTITLE  <b>An Inversion Method for Reconstructing Hall Thruster Plume Parameters from the Line Integrated Measurements (Preprint)</b>		5a. CONTRACT NUMBER		
		5b. GRANT NUMBER		
		5c. PROGRAM ELEMENT NUMBER		
6. AUTHOR(S) Taylor S. Matlock (Jackson and Tull); C. William Larson & William A. Hargus (AFRL/PRSS); Michael R. Nakles (ERC)		5d. PROJECT NUMBER 33SP0706		
		5e. TASK NUMBER		
		5f. WORK UNIT NUMBER		
7. PERFORMING ORGANIZATION NAME(S) AND ADDRESS(ES)  Air Force Research Laboratory (AFMC) AFRL/PRSS 1 Ara Drive Edwards AFB CA 93524-7013		8. PERFORMING ORGANIZATION REPORT NUMBER  AFRL-PR-ED-TP-2007-330		
9. SPONSORING / MONITORING AGENCY NAME(S) AND ADDRESS(ES)  Air Force Research Laboratory (AFMC) AFRL/PRS 5 Pollux Drive Edwards AFB CA 93524-70448		10. SPONSOR/MONITOR'S ACRONYM(S)		
		11. SPONSOR/MONITOR'S NUMBER(S) AFRL-PR-ED-TP-2007-330		
12. DISTRIBUTION / AVAILABILITY STATEMENT  Approved for public release; distribution unlimited (07227A)				
13. SUPPLEMENTARY NOTES For presentation at the 43 <sup>rd</sup> AIAA/ASME/SAE/ASEE Joint Propulsion Conference, Cincinnati, OH, 8-11 July 2007.				
14. ABSTRACT  Utilizing symmetry and extensive datasets, it is possible to extract three-dimensional distributions from two dimensional data. Numerically, these inversions are unstable and prone to magnify noise. However, noise amplification can be controlled by careful addition of artificial smoothing within the numerical inversion algorithm. The precept of Tikhonov regularization is that a unique, stable solution to a deconvolution may be achieved by minimizing a constrained smoothing function. Fundamentally, this will generate a stable, single valued solution only so long as the uncertainty of the iterated solution does not exceed the uncertainty (noise) of the original data. Within these constraints, the algorithm is relatively insensitive to noise. Using Tikhonov deconvolution, it is possible to determine radial profiles from line integrated measurements. A preliminary evaluation of the deconvolution scheme was made with a biased tungsten wire acting as a Faraday probe. After the deconvolution method was assessed, it was applied to a spectroscopic survey of relative xenon neutral line intensities in the near infrared. The radially resolved emission ratios provide a three-dimensional estimate of the plume electron temperature using a published xenon collisional radiative model.				
15. SUBJECT TERMS				
16. SECURITY CLASSIFICATION OF:  a. REPORT Unclassified		17. LIMITATION OF ABSTRACT SAR	18. NUMBER OF PAGES 20	19a. NAME OF RESPONSIBLE PERSON Dr. William A. Hargus  19b. TELEPHONE NUMBER (include area code) N/A
b. ABSTRACT Unclassified				
c. THIS PAGE Unclassified				

# An Inversion Method for Reconstructing Hall Thruster Plume Parameters from Line Integrated Measurements (Preprint)

Taylor S. Matlock\*

*Jackson & Tull, Edwards AFB, CA, 93524*

William A. Hargus Jr.<sup>†</sup> and C. William Larson<sup>‡</sup>

*AFRL/PRSS, Edwards AFB, CA, 93524*

Michael R. Nakles<sup>§</sup>

*ERC, Edwards AFB, CA, 93524<sup>¶</sup>*

Utilizing symmetry and extensive data sets, it is possible to extract three-dimensional distributions from two dimensional data. Numerically, these inversions are unstable and prone to magnify noise. However, noise amplification can be controlled by careful addition of artificial smoothing within the numerical inversion algorithm. The precept of Tikhonov regularization is that a unique, stable solution to a deconvolution may be achieved by minimizing a constrained smoothing function. Fundamentally, this will generate a stable, single valued solution only so long as the uncertainty of the iterated solution does not exceed the uncertainty (noise) of the original data. Within these constraints, the algorithm is relatively insensitive to noise. Using Tikhonov deconvolution, it is possible to determine radial profiles from line integrated measurements. A preliminary evaluation of the deconvolution scheme was made with a biased tungsten wire acting as a Faraday probe. After the deconvolution method was assessed, it was applied to a spectroscopic survey of relative xenon neutral line intensities in the near infrared. The radially resolved emission ratios provide a three-dimensional estimate of the plume electron temperature using a published xenon collisional radiative model.

## I. Introduction

The Hall thruster is a high specific impulse electric thruster that produces a highly ionized plasma inside an annular chamber through the use of high temperature electrons confined by a radial magnetic field across an axial electric field. The characteristics of the near field plasma are of immediate importance to improving and understanding thruster operation and spacecraft integration. Accurate, non-intrusive measurements of near field plume properties are important for both device and plume model validation.

The computed tomographic reconstruction of images from line-of-sight measurements has found widespread use in various forms of non-intrusive diagnostics. Many test environments, however, allow only limited views of the subject, leaving the problem woefully underdetermined. In these applications, a meaningful solution typically requires some prior knowledge of the system. In emission spectroscopy, radial emission profiles are often obtained from projected radiation intensity measurements of an optically thin and cylindrically symmetric plasma.<sup>1,2</sup> Such a problem can be solved analytically by the Abel integral equations. In the discrete

---

\*Engineer, Jackson & Tull, 1 ARA Rd Edwards AFB, CA, 93524, AIAA Member.

<sup>†</sup>Engineer, AFRL/PRSS, 1 ARA Rd Edwards AFB, CA, 93524, AIAA Senior Member.

<sup>‡</sup>Scientist, AFRL/PRSS, 1 ARA Rd Edwards AFB, CA, 93524, AIAA Senior Member.

<sup>§</sup>Engineer, ERC, 1 ARA Rd Edwards AFB, CA, 93524, AIAA Member.

<sup>¶</sup>Distribution A: Approved for public release; distribution unlimited

case presented by experimental data the Abel inversion suffers by requiring the inherent noise amplification of differentiation.

Many methods have been devised to minimize this sensitivity to noise.<sup>3,4</sup> Several procedures involve fitting the data with a smooth function before solving the Abel inversion analytically, with fitting techniques ranging from Taylor series to piecewise cubic splines.<sup>2,5-7</sup> Another method, adopted here, frames the problem as a discrete first order Fredholm integral, inverted by Tikhonov regularization, thus eliminating the need for differentiation.<sup>8</sup> A simple Tikhonov regularization algorithm is put forth here with the purpose of spatially resolving measurements of the cylindrically symmetrical plume of a Hall thruster.

The most common diagnostic of Hall thruster plumes is some variation of the electrostatic probe. Through analysis of the current-voltage characteristics of the plasma, the electrostatic probe can be used to determine fundamental plasma properties.<sup>9</sup> Electrostatic probes are of simple design and are relatively easy to implement, but become problematic in the extreme conditions near the exit plane. High temperatures and densities in the near field and the prominence of thruster magnetic fields can deleteriously affect the probe, which itself induces perturbations in the local plasma, and the interpretation of the current-voltage characteristics.

Optical techniques may be employed to avoid these pitfalls.<sup>10-12</sup> Emission spectroscopy is a useful non-invasive diagnostic, but it is typically limited to line-of-sight interrogations. Here, we use spectroscopic measurements deconvolved via Tikhonov regularization to map out the radial and axial plume emissions in the near infrared spectrum. The collisional radiative model (CRM) of Karabadzhak et al. was applied to determine the electron temperature distribution of the near field of a low power Hall thruster.<sup>13</sup> The spectroscopic measurements were performed following the construction of a new electrostatic probe which provided an initial assessment of the applicability of Tikhonov regularization to Hall thruster plume measurements. The probe, which consists of a taut, partially insulated tungsten wire, biased to the ion saturation regime (-30 V), acts as a Faraday probe integrated along the line-of-sight of the optical system.

## II. Inversion and Regularization

The Abel integral may be derived from a simple geometric case as illustrated in Fig 1. The radially dependent function of interest,  $f(r)$ , is represented at a given axial location by a circle of radius  $R$ , where  $f(r > R) = 0$ . The measured value,  $b(y)$ , is simply  $f(r)$  integrated along  $x$ . If the function is symmetric about the  $y$ -axis, the measured value is related to the unknown function by Eqn 1. The common form of the Abel integral, shown in Eqn 2, is obtained by converting  $r$  to its Cartesian components.

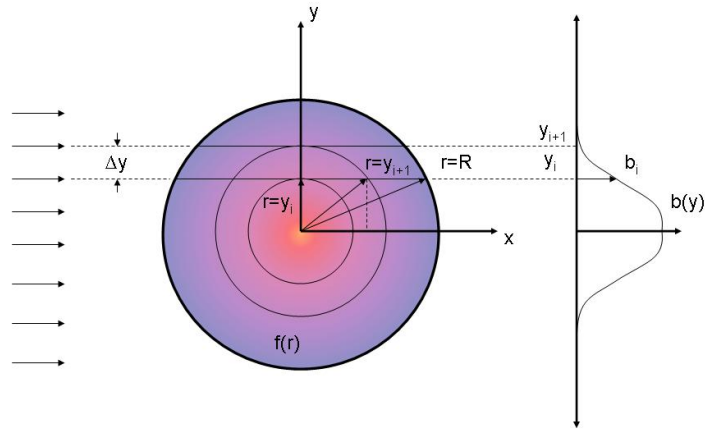


Figure 1. Parallel beam geometry through a cylindrically symmetric test section

$$b(y) = 2 \int_{r=y}^{r=R} f(r) dx \quad (1)$$

$$b(y) = 2 \int_y^R f(r) \frac{r}{\sqrt{r^2 - y^2}} dr \quad (2)$$

The Abel inversion, given in Eqn 3, is an exact analytical solution of  $f(r)$ .<sup>1</sup> As previously noted, experimental data are discrete and contain inherent random errors which often lead to large oscillations when differentiated. The ill-posed nature of the problem precludes the use of simple analytical numerical methods, such as linear least squares or LU decomposition, and instead necessitates the inclusion of noise dampening within the solution procedure.

$$f(r) = -\frac{1}{\pi} \int_r^R \frac{b'(y)}{\sqrt{y^2 - r^2}} dy \quad (3)$$

Equation 2 is a Fredholm integral of the first kind which has the matrix form shown in Eqn 4, where  $\mathbf{A}$  is the kernel, and  $\mathbf{b}$  is the known convolution of the kernel and some unknown function of arbitrary size. We formulate the kernel using a common collocation method, likened to concentric shells of constant  $f_i$ , shown in Eqn 5, resulting in the discrete, right triangular kernel of Eqn 6.<sup>8,14,15</sup> A well formed kernel is essential to the success of deconvolution, which has led to the accumulation of literature on its analysis, particularly through singular value decomposition.<sup>16-18</sup>

$$\mathbf{A}_{M \times N} \cdot \mathbf{f}_{N \times 1} = \mathbf{b}_{M \times 1}, \quad N \leq M \quad (4)$$

$$b_i = \sum_{j=i}^{n-1} \left[ 2f_j \int_{y_j}^{y_{j+1}} \frac{r}{\sqrt{r^2 - y^2}} dr \right] = \sum_{j=i}^{n-1} \left[ 2f_j \left[ \sqrt{r^2 - y^2} \right]_{y_j}^{y_{j+1}} \right] \quad (5)$$

$$\mathbf{A}_{m,n} = 2 \left[ \sqrt{[(n+1)\Delta r]^2 - (m\Delta y)^2} - \sqrt{(n\Delta r)^2 - (m\Delta y)^2} \right] \quad (6)$$

The classical regularization method developed by and named after Andrei Tikhonov finds a stable solution to the inverse problem by balancing the quality of fit with a smoothing constraint. The most general form of Tikhonov regularization is the minimization problem shown in Eqn 7, where  $\lambda$  is a regularization parameter greater than zero,  $L$  is a regularization operator, and  $f_0$  is an *a priori* estimate of the unknown function, here set to zero.<sup>19</sup> The formal solution proposed by Tikhonov is shown in Eqn 8.

$$\min\{\|Af - b\|_2^2 + \lambda^2 \|L(f - f_0)\|_2^2\} \quad (7)$$

$$f_\lambda = (A^T A + \lambda^2 L^T L)^{-1} (A^T b + \lambda^2 L^T L f_0) \quad (8)$$

The regularization operator is left to the discretion of the user, but is, in its standard form, some order of discrete approximation to the derivative. The zeroth order operator is simply the  $n \times n$  identity matrix, and is used to limit the size of the solution. The first order operator, adopted here, is the  $(n-1) \times n$  band diagonal matrix shown in Eqn 9, which may be used to constrain the solution towards a constant.<sup>8,20</sup> Higher order operators have also found application, however the first order operator is sufficient for our case, which assumes diffusion in the plasma will tend to minimize gradients in the plume.

$$L^{(1)} = \begin{bmatrix} -1 & 1 & 0 & \dots & 0 \\ 0 & -1 & 1 & \dots & 0 \\ 0 & & & & \\ \vdots & & & & \\ 0 & 0 & \dots & -1 & 1 \end{bmatrix} \quad (9)$$

Choice of the regularization parameter is one of the more controversial aspects of Tikhonov regularization. A number of optimization techniques exist, each with their own benefits and drawbacks.<sup>8,17,21</sup> This work makes use of a simple and visually elucidating aid known as the L-curve. The L-curve is produced by plotting the smoothing norm,  $\|L(f - f_0)\|$ , versus the residual norm,  $\|Af_\lambda - b\|$ , on a log-log axis for various values of the regularization parameter. Figure 3 shows an example L-curve, which provides a visual representation of the trade-offs between the smoothing constraint and the least squares solution. Most theories propose an

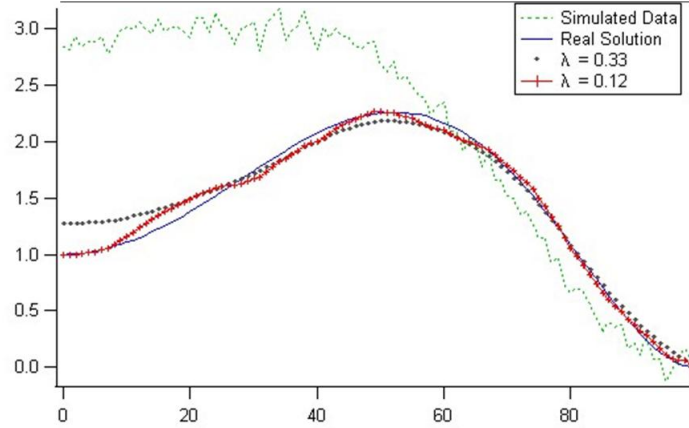


Figure 2. Deconvolution results for Holloway test case with 3% Gaussian noise

optimal parameter exists at the “corner” of the L-curve, but studies have shown that this tends to oversmooth the solution.<sup>19</sup>

Several test cases were run using our Tikhonov deconvolution algorithm, in order to examine the efficacy of the L-curve and routine parameters in general. The first test case examined was detailed by Holloway et al. as a test for their Abel inversion routine. It simulates a cylindrically symmetric plasma emission coefficient given by the sixth order polynomial test function in Eqn 10.<sup>8</sup> The second test case studied made use of a normalized Gaussian curve, with a FWHM of  $N/2$ , to simulate the large gradients expected in the near field of the Hall thruster plume.

$$f(r) = 1 + 10r^2 - 23r^4 + 12r^6 \quad (10)$$

The results of our first order Tikhonov deconvolution for the Holloway test case ( $M=N=100$ ), with 3% random Gaussian noise added at each point, are shown in Fig 2 along with the simulated values of  $b$  and the analytically exact solution. The L-curve for this particular case is shown in Fig 3, where the boxed regularization parameter is the so-called corner and the circled point corresponds to the minimal error solution, lending credence to the theory that the L-curve corner may result in an oversmoothed solution.

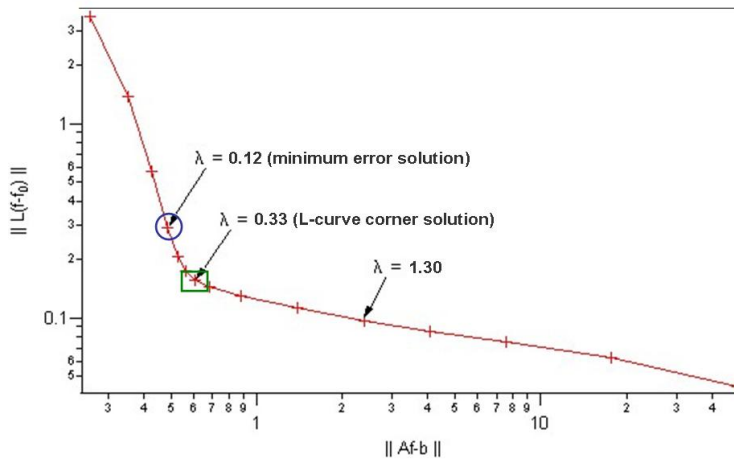


Figure 3. L-curve for Holloway test case with 3% Gaussian noise

The size of the solution ( $N$ ) is also left to the discretion of the user (so long as  $N \leq M$ ), so  $N$  was varied to

determine its effects, if any, on convergence. A plot showing the true residual norm and optimal regularization parameters normalized by  $N$  as functions of  $N$ , averaged over 50 samples of the Holloway test case with 3% added noise and  $M=100$ , is shown in Fig 4. The results show that the accuracy of the best solution is generally independent of size for  $N$  greater than 20% of  $M$ .

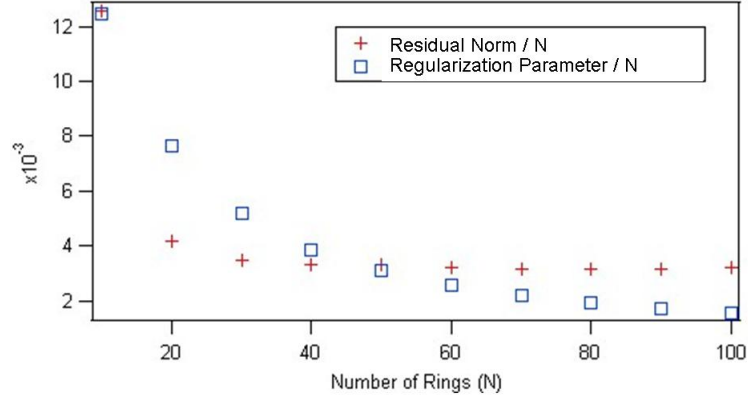


Figure 4. Normalized residual and regularization parameter versus solution size for Holloway test case with 3% Gaussian noise

The effects of noise on our solution was investigated by varying the percentage of added Gaussian noise. The regularization parameter yielding the smallest residual between our deconvolved solution and the analytical solution is shown versus noise in Fig 5, averaged over 10 samples of the Holloway test case at  $M=N=100$ . The rise in the value of the regularization parameter with noise is expected since more smoothing is necessary as the data loses fidelity. The total error in the data can be described by the residual norm between the ideal right hand side,  $b^0$ , and the noisy data,  $b^{noise}$ . The total error is plotted alongside the residual norm from the L-curve in Fig 5 for varied levels of noise. The equivalence of these two norms is predicted by V.A. Morozov's discrepancy principle.<sup>22</sup> The discrepancy principle can be used to select the optimal regularization parameter when the error in the data can be accurately bounded, as illustrated in Fig 5.

The second test case used was a Gaussian distribution with Gaussian noise added point by point. The exact analytical solution (0% noise) was calculated using Eqn 3. Sample deconvolution results are shown in Fig 6 using both the optimal and L-curve derived regularization parameter, with the L-curve itself displayed in Fig 7, for  $M=N=100$  at 3% noise. The Gaussian test case demonstrates the tendency of the regularization algorithm to underestimate the peak in order to dampen oscillations elsewhere. The Gaussian and Holloway test cases represent the distributions expected in the thruster plasma. The Holloway test case demonstrated that for small gradients we can reliably choose the L-curve corner for slightly oversmoothed solutions, while the Gaussian case led to the expectation of underestimated peak heights when using the L-curve corner to regularize large gradients.

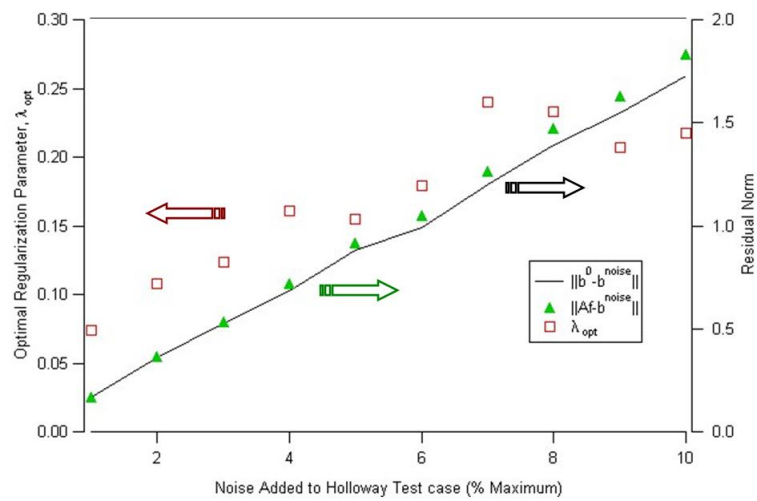


Figure 5. Optimal regularization parameter versus added noise for Holloway test case

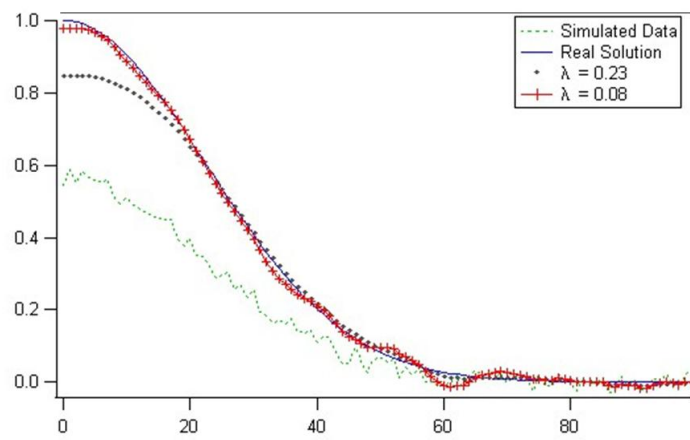


Figure 6. Deconvolution results for Gaussian test case with 3% Gaussian noise

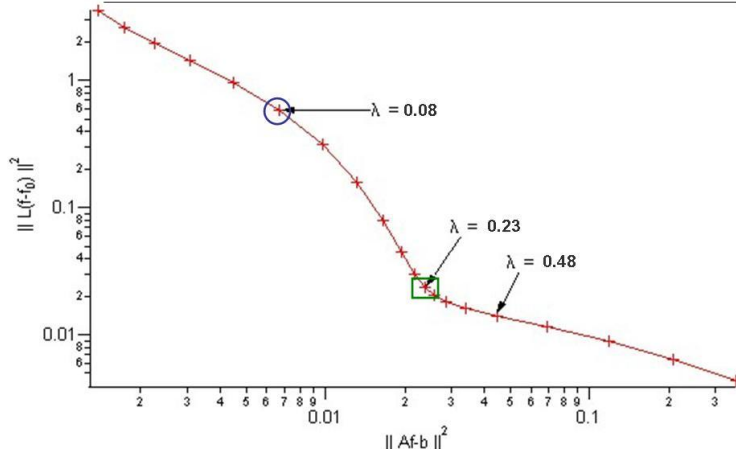


Figure 7. L-curve for Gaussian test case with 3% Gaussian noise

### III. Experimental Setup

#### A. Hall Thrusters

The Hall thruster examined in this study is the 200 W Busek Company, Inc. BHT-200 laboratory Hall thruster, shown integrated inside AFRL Chamber 6 in Fig. 8 with the wire probe at its lateral origin. The nominal thruster operating conditions are shown in Table 1. A prominent feature of this Hall thruster is the central nose cone, which protrudes about 7mm from the exit plane, impeding the collection of light near the measurement origin. A more detailed description of the Hall thruster is given elsewhere.<sup>23</sup>

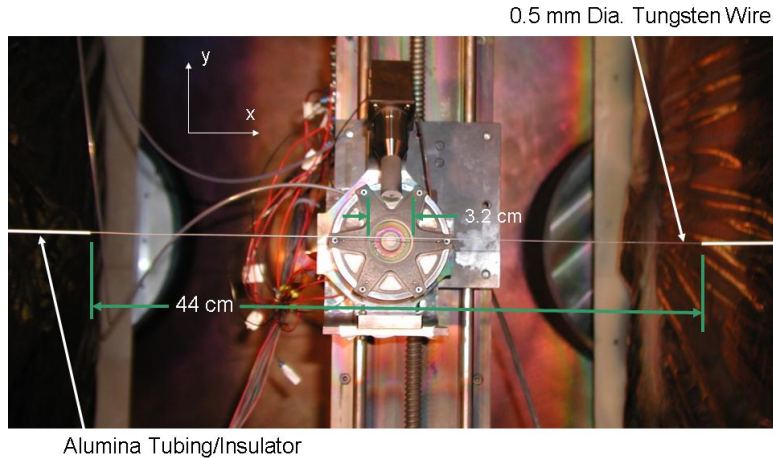


Figure 8. Hall thruster installed in Chamber 6 with the thin wire ion flux probe

#### B. Laboratory Facilities

All testing was performed in Chamber 6 at the Air Force Research Laboratory Electric Propulsion Laboratory at Edwards AFB, CA. This chamber is constructed of nonmagnetic stainless steel with a 1.8 m diameter and 3.0 m length. Four single stage cryo-panels ( $\sim 25$  K) and one 50 cm two stage cryo-pump ( $< 12$  K) provide a measured pumping speed of 32,000 l/s on xenon. The chamber is roughed by an oil free Stokes mechanical pump and blower. Background pressure in the chamber, measured by an ionization gauge,

Anode flow	840 $\mu\text{g/s}$ (Xe)
Cathode flow	98 $\mu\text{g/s}$ (Xe)
Anode potential	250 V
Anode current	0.85 A
Keeper current	0.5 A
Magnet current	1.0 A
Heater current	3.0 A

**Table 1. Hall thruster nominal operating conditions<sup>23</sup>**

reached a maximum of 0.8 mPa, corrected for xenon, during Hall thruster operation. Graphite panels were installed on several interior surfaces as a precautionary measure to minimize sputtering from the stainless steel chamber walls.

The thruster was installed on a three-axis positioning system, comprising of three orthogonal translation stages controlled through a National Instruments interface. In this study, only the y and z axes were used. The y-axis translation stage moves the thruster to different positions above and below each of the stationary, line-of-sight probes, while the z-axis stage controls the axial separation of thruster and probe.

### C. Diagnostic Apparatus

The inversion method described is used to spatially resolve data from a thin wire ion flux probe as well as line-of-sight spectroscopic measurements. The thin wire ion flux probe was developed as a precursor to the spectroscopic measurements, in order to assess the inversion algorithm.

The wire probe, shown in Fig 8, consists of 66 cm of 0.5 mm diameter tungsten wire in tension, insulated at each end by 11 cm of alumina tubing, leaving 44 cm of the wire exposed to the plasma plume. The tungsten wire was biased to -30 V with respect to the chamber, in order to only collect current in the ion saturation regime. The collected current, which was averaged over ten samples at each position, is proportional to the integrated current density and the area over which it is collected. The bare wire length was determined by the range of the y-axis stage and the need to ensure the current collected at y=R approached zero.

Line integrated emission measurements were obtained using an Ocean Optics USB2000 Spectrometer (42 mm focal length, 400-1100 nm, 2048 elements). The spectrometer was attached to an air-spaced doublet collimator, optimized for 650-1050 nm, via one of two fiber optic cables (50  $\mu\text{m}$  or 600  $\mu\text{m}$  diameter). The collimator viewed the plasma through a glass viewport, with a field stop ( $\sim$ 3 mm) placed 82 cm from the collimator and 28 cm from the thruster central axis, as shown schematically in Fig 9. The beam divergence through the optical assembly was tested with a HeNe laser, which revealed a 3 mm diameter beam on the thruster side of the aperture, with a divergence half angle of 3° for the 600  $\mu\text{m}$  fiber. An approximately 3 mm diameter beam was measured with the 50  $\mu\text{m}$  fiber, with negligible divergence up to 50 cm from the aperture.

A wavelength calibration was performed using a mercury discharge lamp and an intensity calibration was performed using a calibrated 200 W quartz halogen, tungsten filament lamp placed in the position of the thruster, and measured through the optical apparatus. The standard deviation in intensity measurements between 820 and 830 nm were less than 1% after calibration with the 600  $\mu\text{m}$  fiber, and less than 3% with the 50  $\mu\text{m}$  fiber. All optical measurements were corrected for dark noise and normalized by integration time.

The line-of-sight intensity measurements from the spectrometer were spatially resolved by the inversion method for several near infrared (NIR) lines with a dependence on electron temperature, enumerated by Karabadzhak et al.<sup>13</sup> The intensity ratio between the lines at 823.2 and 828.0 nm was modelled for the 200 W thruster operating conditions as a function of electron temperature. The results, which can yield temperature estimates from 1 to 20 eV with confidence, are displayed in Fig 10.<sup>24</sup> The curve in Fig 10 shows low sensitivity to error for temperatures between about 1 and 4 eV. When the temperature exceeds  $\sim$ 8 eV, a 3% error in the measured intensity ratio can result in more than 6% error in the calculated temperature.

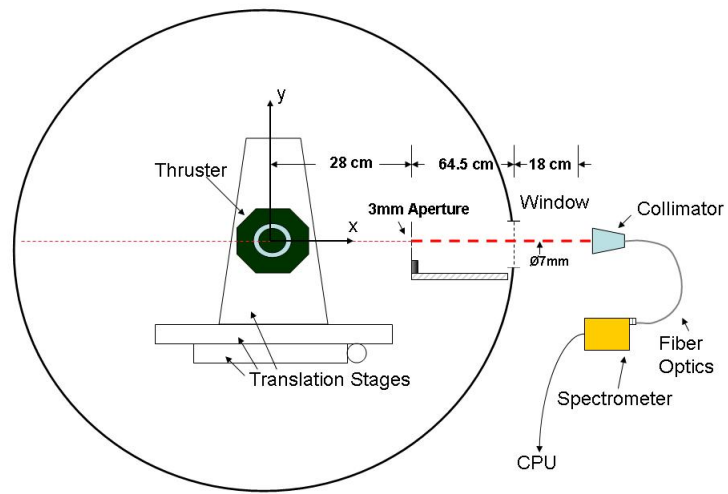


Figure 9. Optical apparatus for Hall thruster emission spectroscopy

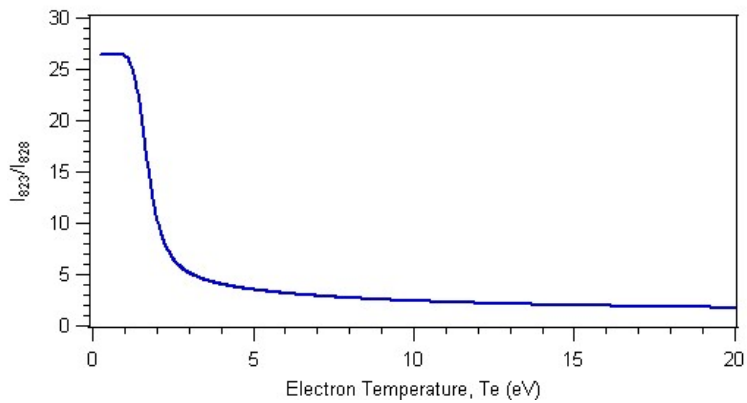
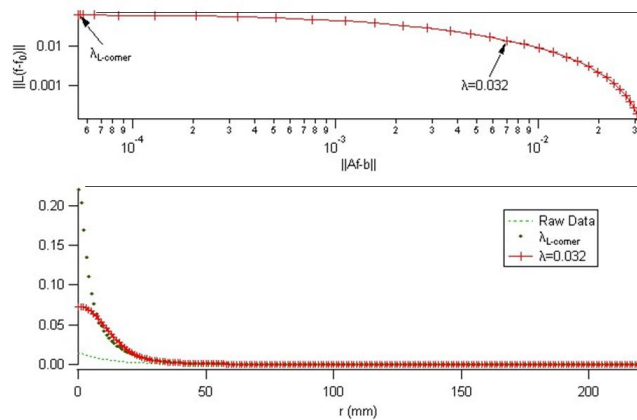


Figure 10. Calculated electron temperature dependence of the intensity ratios of the XeI 828.0 and 823.2 nm lines<sup>24</sup>

## IV. Results

The wire probe provides a straight forward method for gauging how symmetric the ion current is about the thruster central axis. A survey of the Hall thruster plume revealed only minor asymmetry between the cathode and non-cathode sides at axial distances from 1 to 9 times the outer diameter of the annulus (OD=3.2 cm) downstream of the exit plane. The mildness of the asymmetry allows application of the Abel kernel to the average of the two sides for axial positions downstream of the cathode ( $z>0.85$  OD).

Measurements made by the wire probe close to the thruster contained high gradient central peaks. This complicated application of the inversion algorithm. The L-curve for the first order Tikhonov would not converge on an optimal parameter because the gradients were too large to come to a significant balance with the least-squares solution. The non-convergence of the L-curve close to the thruster, displayed in Fig 11, led to the use of the discrepancy principle to find an appropriate regularization parameter. The total error in the wire probe measurements is not known, so an estimate was made that the error in each point was less than or equal to the minimum current measured in the plume. The discrepancy principle matched the L-curve in promoting the use of the unregularized, least squares solution at 1 OD.



**Figure 11.** Wire probe measurements of the Hall thruster 1 OD downstream, with the inverse using an optimal and off-optimal regularization parameter. The L-curve is shown above. Here  $\lambda_{L\text{-corner}}=\lambda_{discrepancy}$ .

At axial positions further downstream ( $z>1$  OD), the two parameter selection methods began to diverge, as shown in Fig 12. The L-curve comes to a very shallow corner near  $\lambda=0$ , leading to an unsmoothed solution. The discrepancy principle yields a non-zero parameter, which over-smooths the off-center peak given by the least-squares solution.

The L-curve finally converges to a non-trivial regularization parameter at a distance of 9 OD. At this distance the discrepancy principle parameter appears to over-smooth the solution once again, completely removing the off-center peak in the L-curve solution. The discrepancy principle parameter location on the L-curve points to an overestimation of the error in the data, so the L-curve criterion was used to deconvolve the spatial image of the plume shown in Fig 14, with corrections made for the current collection area.

Faraday probe data was available for the Hall thruster, at axial distances greater than 3 OD, from previous testing done in AFRL Chamber 6.<sup>25</sup> In order to compare the two data sets, collection area must be accounted for in the deconvolved wire probe measurements. Double probe measurements of the thruster, also performed in Chamber 6 at  $z>3$  OD, support the thin sheath assumption near the center of the wire, but Debye lengths on the order of the wire diameter were found near the edges.<sup>25</sup> Sheath thicknesses ( $x_s$ ) were estimated from Debye length ( $\lambda_d$ ) measurements using the relationship given by Hutchinson calculated for Xenon ( $x_s \sim 5.3\lambda_d$ ).<sup>26</sup> A second order polynomial was then fit to the sheath thickness estimates in order to calculate an effective collection circumference as a function of position along the wire. The sheath thickness curve-fit predicted sheath sizes ranging from 0.1 mm at the center to 1.6 mm at the edges.

The current densities deconvolved from wire probe data and normalized by collection area were higher than Faraday probe measurements near the thruster centerline by 25% on average, as shown in Fig 15. Wire

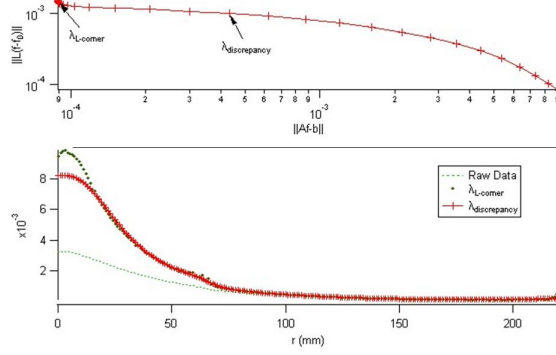


Figure 12. Wire probe measurements of the Hall thruster 5 OD downstream, with the inverses using the L-curve corner and discrepancy principle. The L-curve is shown above.

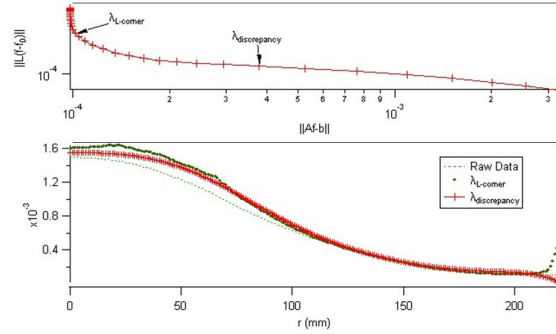


Figure 13. Wire probe measurements of the Hall thruster 9 OD downstream, with the inverses using the L-curve corner and discrepancy principle. The L-curve is shown above.

probe measurements outside of the peaks were typically less than Faraday probe data by approximately 10%. Most of the uncertainty in the wire probe data comes not from the inversion method, but the collection area model. If the minimum sheath thickness from the double probe (.05 mm) is used instead of the curve-fit value, current densities increase by 9%.

Following wire probe testing, the wire was examined for evidence of erosion. The wire retained its 0.5 mm diameter near its ends, but diameters as low as 0.4 mm were measured at the probe center. Wire erosion was only measureable up to one outer diameter from the center. The total estimated area of exposed wire decreased by only 1.5% over roughly 40 hours of testing, assuming a monotonic decrease in wire diameter near the center. However, an estimated 10% of the wire area had eroded within 1 OD of the center, the portion where the highest current densities were measured, with approximately 2 of the 40 hours of exposure spent within 1 OD of the exit plane.

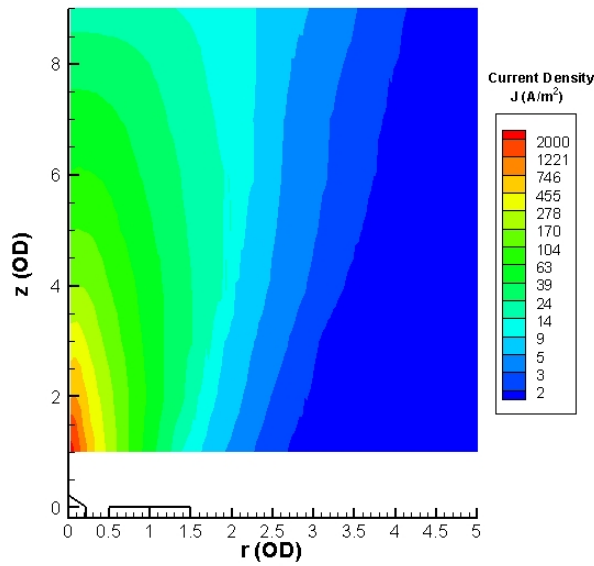


Figure 14. Wire Probe Data inversion for the Hall thruster using the L-curve corner and a variable sheath thickness

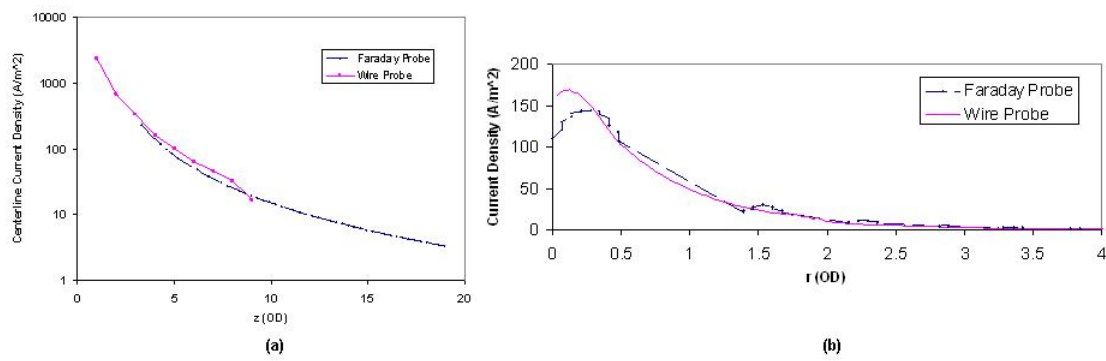


Figure 15. (a) Current densities along the centerline given by wire probe data inversion and Faraday probe measurements for the Hall thruster using the L-curve corner and a sheath thickness of 0.1 mm (b) Radial current density profiles at  $z=4$  OD from Faraday probe measurements and wire probe data inversion using a variable sheath thickness

## A. Emission Spectroscopy

Spectra were recorded from -1 to 1 OD with 1/8 OD steps along the y-axis, from the exit plane to 1 OD downstream at 1/4 OD increments using the 600  $\mu\text{m}$  fiber. A finer lateral mesh was obtained with the 50  $\mu\text{m}$  fiber, at 1/16 OD increments, with axial measurements extending to 5/4 OD at 1/4 OD intervals. Several measurements were made in which light collection was impeded by the central nose cone of the thruster. A new kernel was calculated for these measurements which accounted for the effective optical path. A face plate mounting bolt was removed from the thruster in order to view the nose cone at the measurement origin.

Unlike the wire probe experiment, cathode side emission could not be averaged with lower half data due to large asymmetries. The 823.2 and 828.0 nm XeI raw line intensity maps in Fig 16 reveal a point source at the cathode position ( $y \approx 1$  OD,  $z \approx 0.6$  OD) with higher intensities on the cathode side for each of the two optical fibers. Data were typically taken at larger lateral steps with the 600  $\mu\text{m}$  fiber, because of its larger cross-sectional area of integration. Several data sets were recorded with each fiber configuration. Less variation between tests was found with the larger fiber, though both configurations experienced large fluctuations capturing emission of the non-equilibrium plasma at the exit plane.

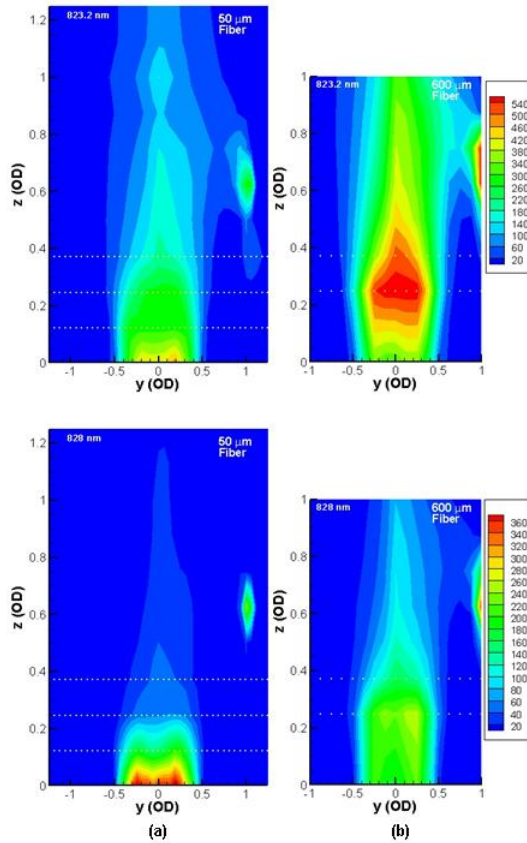
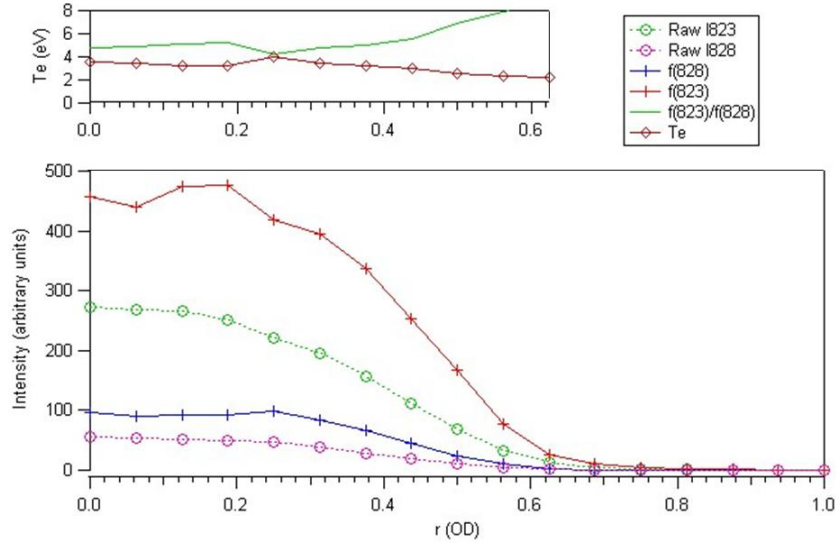


Figure 16. Raw 823.2 and 828.0 nm XeI line intensities in the Hall thruster plume. Measured through a (a) 50  $\mu\text{m}$  diameter optical fiber (b) 600  $\mu\text{m}$  diameter optical fiber with a coarser mesh.

The 823.2 and 828.0 nm line intensities were separately inverted, the results of which are shown in Fig 18, and the ratio of the deconvolved data was applied to the curve in Fig 10 in order to estimate spatially resolved electron temperatures. The deconvolution encountered the same problem of L-curve non-convergence discovered in the wire probe experiments, and once again the unregularized solution was relied on in most cases, as shown in Fig 17. As the measured intensities decreased the discrepancy principle became applicable, always promoting more smoothing on the 828 nm inversions, as expected for their lower signal-to-noise.

The spatially resolved temperatures from both fiber optic configurations are shown in Fig 19 and reveal some similar trends and results. Both fibers measured high temperatures moving from the discharge chamber



**Figure 17.** Raw and inverted 823.2 and 828.0nm XeI line intensities in the Hall thruster plume are used to calculate the electron temperature. Measured just beyond the nose cone tip ( $y=0$ ,  $z=0.25$  OD) through a  $50\text{ }\mu\text{m}$  diameter optical fiber.

towards the centerline, with more dramatic cooling found by the smaller fiber near the nose cone tip. The largest discrepancy between data from the two fiber configurations occurs in the measurement of a smooth, monotonic axial decrease in temperature by the  $600\text{ }\mu\text{m}$  fiber, as compared to the largely oscillatory downstream flow found by the smaller fiber. This difference may be due to the larger signal volume of the  $600\text{ }\mu\text{m}$  fiber, which causes more spatial smoothing of the data.

Both optical configurations measure high temperatures at the exit plane, which approach BHT-200 device plasma simulation predictions, shown in Fig 20.<sup>27</sup> The high electron temperatures near the nose cone may be related to the high nose cone heating observed thermographically in a previous study, and could greatly affect the thruster lifetime if temperatures are high enough to alter the erosion regime.<sup>28</sup> Further downstream, the optical temperature data more closely resemble Langmuir probe data, displayed in Fig 21, than the model. Data from both fiber configurations predict higher temperatures along the centerline and lower temperatures downstream of the annulus than the Langmuir probe, with differences as high as 40%.

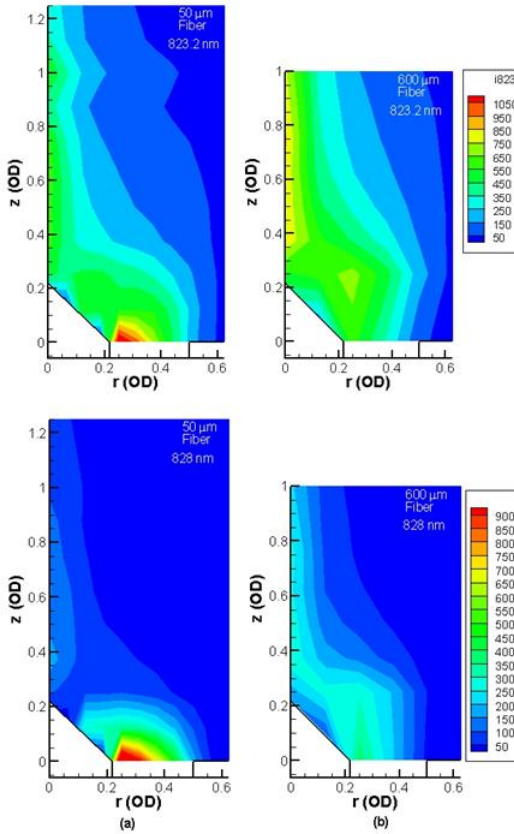


Figure 18. Inverted line intensity distributions at 823.2 and 828.0 nm in the Hall thruster plume. Measured through a (a) 50  $\mu\text{m}$  diameter optical fiber (b) 600  $\mu\text{m}$  diameter optical fiber.

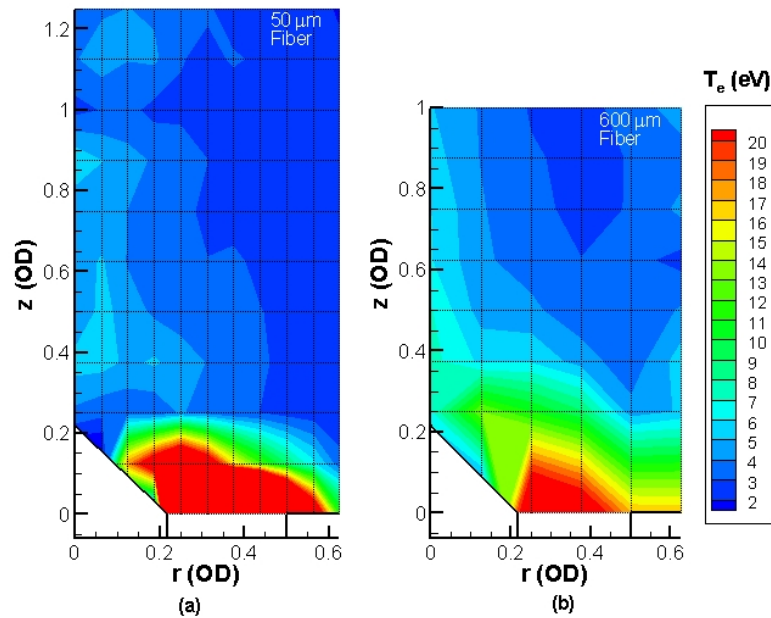


Figure 19. CRM predicted temperatures from inverted 823.2 and 828.0nm XeI intensity ratios in the Hall thruster plume. Measured through a (a)  $50 \mu\text{m}$  diameter optical fiber (b)  $600 \mu\text{m}$  diameter optical fiber, shown with the data mesh superimposed

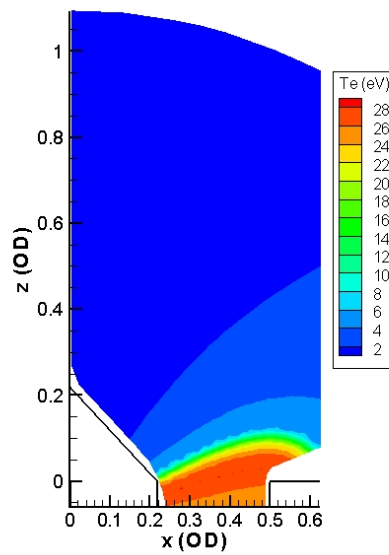


Figure 20. HP Hall model predicted electron temperatures for the Hall thruster<sup>27</sup>

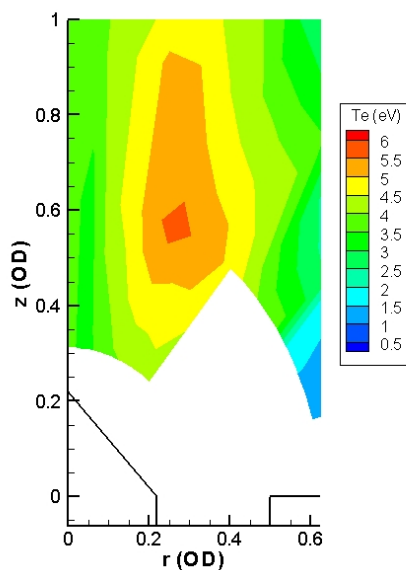


Figure 21. Langmuir probe measured electron temperatures for the Hall thruster<sup>25</sup>

## V. Conclusions and Future Studies

Non-invasive diagnostics, usually limited to line-of-sight measurements, can be spatially resolved using the inversion method presented here. The inversion algorithm was applied successfully to several cases of simulated data as well as a thin wire ion flux probe, and emission spectroscopy data. The method is simple to apply and requires no other *a priori* information than the aptness of the cylindrical symmetry assumption.

It was shown that the L-Curve is useful for visualizing trade-offs during regularization, but typically ineffective in its application to the near-field of a low power Hall thruster plume. The discrepancy principle was also found to be useful in an indicative if not practicable manner. Both tools showed the very near field plume to yield a signal-to-noise ratio high enough to preclude the use of regularization. Simulated test cases demonstrated the efficacy of the regularization method at noise levels much higher than those encountered experimentally. Future studies of the inversion algorithm may include the use of new regularization parameter selection methods, different collocations of the kernel, and comparison with the explicit Abel solution of curve fits.

The wire probe provided an intriguing study of both plume mechanics and inversion methods. Good agreement was found between deconvolved wire probe measurements and spatial Faraday probe data under certain assumptions of sheath characteristics. The physical processes involved in wire probe current collection add an as yet underdetermined element impeding its use as a plasma diagnostic, though warranting further study. The most important precursor to further wire probe experiments is a well-defined model of the thin wire current collection.

Future experiments will involve the replacement of the thin wire with a flat conductive strip of larger surface area in an attempt to create a more uniform sheath. Excessive heating of the wire may create an unwanted current source due to thermionic emission, which, along with erosion and impingement effects, may be mitigated by decreasing plume exposure time.

The spectroscopic measurements provide insight into the thruster plasma in a non-invasive manner. CRM derived temperature measurements were reliably obtained in the high signal-to-noise regions along the thruster axis in the near-field, although data typically exceeded the on-axis values expected by simulations and Langmuir probe analysis.<sup>13,25</sup> General temperature distribution trends were shown to be largely unaffected by alterations in the optical configuration. The CRM is currently limited in its range and accuracy, but as the model expands so too will the applicability of this diagnostic.

Further analysis of the spectroscopic results is underway, in order to complete the characterization of errors in the current system. The effects of the optical geometry are yet to be fully quantified, as are the uncertainties involved in the deconvolving of temperature from intensity ratios. Tikhonov regularization may also be used to deconvolve line shapes from the instrument function of the spectrometer.

Future optical tests may use different combinations of lines to infer temperatures as well as different viewing angles. CCD images were obtained with filters intended to separate the lines at 823.2 and 828.0 nm, but were unsuccesful. Future tests may make use of a properly filtered CCD camera for temporal, spatially resolved temperature measurements.

## VI. Acknowledgements

The authors would like to thank Dr. Rainer Dressler of AFRL/VS for the invaluable assistance in calculating and applying the CRM. The authors would also like to thank Garrett Reed for his help in setting up the experiments.

## References

<sup>1</sup>Barr, W., "Method for Computing the Radial Distributioon of Emitters in a Cylindrical Source," *Journal of the Optical Society of America*, 1961.

<sup>2</sup>Li, X., Huang, L., and Huang, Y., "A new Abel inversion by means of the integrals of an input function with noise," *Journal of Physics A: Mathematical and Theoretical*, 2007.

<sup>3</sup>Asaki, T., Chartrand, R., Vixie, K., and Wohlberg, B., "Abel inversion using total variation regularization," *Institute of Physics Publishing*, 2005.

<sup>4</sup>Nunes, F., Santos, J., and Manso, M., "Recursive algorithm for fast evaluation of the Abel inversion integral in broadband reflectometry," *Review of Scientific Instruments*, 1998.

<sup>5</sup>Deutsch, M. and Beniaminy, I., "Inversion of Abel's integral equation for experimental data," *Journal of Applied Physics*, 1983.

<sup>6</sup>Freeman, M. and Katz, S., "Determination of a Radiance-Coefficient Profile from the Observed Asymmetric Radiance Distribution of an Optically Thin Radiating Medium," *Journal of the Optical Society of America*, 1963.

<sup>7</sup>Glasser, J., Chapelle, J., and Boettner, J., "Abel inversion applied to plasma spectroscopy: a new interactive method," *Journal of Applied Optics*, 1978.

<sup>8</sup>Holloway, J., Shannon, S., Sepke, S., and Brake, M., "A reconstruction algorithm for a spatially resolved plasma optical emission spectroscopy sensor," *Journal of Quantitative Spectroscopy and Radiative Transfer*, 1999.

<sup>9</sup>Lieberman, M. and Lichtenberg, A., *Principles of Plasma Dishchares and Materials Processing*, Wiley Interscience, 1994.

<sup>10</sup>Hargus, W. and Cappelli, M., "Laser-Induced Fluorescence measurements on a laboratory Hall Thruster," *34th AIAA/ASME/SAE/ASEE Joint Propulsion Conference*, Cleveland, OH, July 1998.

<sup>11</sup>Hargus, W., "Laser-Induced Fluorescence of Neutral Xenon in the Near Field of a 200 W Hall Thruster," *41st AIAA/ASME/SAE/ASEE Joint Propulsion Conference*, Tucson, AZ, July 2005.

<sup>12</sup>Manzella, D., "Stationary Plasma Thruster Plume Emissions," *23rd IEPC*, Seattle, WA, September 1993.

<sup>13</sup>Karabadzhak, G., Chiu, Y., and Dressler, R., "Passive optical diagnostic of Xe propelled Hall thrusters; II. Collisional-radiative model," *Journal of Applied Physics*, 2006.

<sup>14</sup>Aguilera, J., Aragon, C., and Bengoechea, J., "Spatial characterization of laser-induced plasmas by deconvolution of spatially resolved spectra," *Journal of Applied Optics*, 2003.

<sup>15</sup>Hanna, G., Roumeliotis, J., and Kucera, A., "Collocation and Fredholm Integral Equations of the First Kind," *Journal of Inequalities in Pure and Applied Mathematics*, 2005.

<sup>16</sup>Hansen, P., "Numerical tools for analysis and solution of Fredholm integral equations of the first kind," *Inverse Problems* 8, 2001.

<sup>17</sup>O'Leary, D., "Near-Optimal Parameters for Tikhonov and Other Regularization Methods," *Journal of Scientific Computing*, 2001.

<sup>18</sup>Vogel, C., "Non-convergence of the L-curve regularization parameter selection method," *Inverse Problems* 12, 1996.

<sup>19</sup>Hansen, P., "The L-curve and its use in the numerical treatment of inverse problems," *Computational Inverse Problems in Electrocardiology*, 2001.

<sup>20</sup>Power, J., "Linear Tikhonov regularization against an edge field: an improved reconstruction algorithm in photothermal depth profilometry," *Applied Physics B*, 2003.

<sup>21</sup>Benck, E. and Etemadi, K., "Fiber Optic Based Optical Tomography Sensor for Monitoring Plasma Uniformity," 2000.

<sup>22</sup>Nair, M., Schock, E., and Tautenhahn, U., "Morozov's Discrepancy Principle under General Source Conditions," *Journal for Analysis and its Applications*, 2003.

<sup>23</sup>Hargus, W. and Reed, G., "The Air Force Clustered Hall Thruster Program," *38th Joint Propulsion Conference*, AIAA-2002-3678, July 2002.

<sup>24</sup>Personal communication, Rainer Dressler, May 9, 2007.

<sup>25</sup>Nakles, M., Reed, G., and Hargus, W., "Experimental and Numerical Examination of the BHT-200-X3 Hall Thruster Plume," *43rd AIAA/ASME/SAE/ASEE Joint Propulsion Conference*, Cincinnati, OH, July 2007.

<sup>26</sup>Hutchinson, I., *Principles of Plasma Diagnostics*, Cambridge University Press, 1987.

<sup>27</sup>Nakles, M., Hargus, W., and G, D., "Comparison of Numerical and Experimental Near-Field Ion Velocity Distributions of the BHT-200-X3 Hall Thruster," *42rd AIAA/ASME/SAE/ASEE Joint Propulsion Conference*, Sacramento, CA, July 2006.

<sup>28</sup>Matlock, T., Hargus, W., and Larson, C., "Thermographic Characterization and Comparison of 200W and 600W Hall Thrusters," *43rd AIAA/ASME/SAE/ASEE Joint Propulsion Conference*, Cincinnati, OH, July 2007.